Nanoscale

PAPER

View Article Online
View Journal | View Issue

Cite this: *Nanoscale*, 2015, **7**, 11082

Functionalized ZnO@TiO_2 nanorod array film loaded with $ZnIn_{0.25}Cu_{0.02}S_{1.395}$ solid-solution: synthesis, characterization and enhanced visible light driven water splitting†

Ruosong Wang,[a] Xiaoxue Xu,[b,d] Yi Zhang,[a] Zhimin Chang,[a] Zaicheng Sun*[c] and Wen-Fei Dong*[a]

Received 2nd April 2015,
Accepted 15th May 2015

DOI: 10.1039/c5nr02127h

www.rsc.org/nanoscale

We have designed a novel semiconductor core/layer nanostructure of a uniform ZnO@TiO_2 nanorod array modified with a $ZnIn_{0.25}Cu_{0.02}S_{1.395}$ solid-solution on the surface *via* a facile hydrothermal synthesis. This novel nanostructure combines the merits of all components and meets the requirements of photovoltaic system application. An intimate PN heterojunction is formed from the ZnO@TiO_2 nanorod and polymetallic sulphide solid-solution, which is remarkably beneficial for the effective visible light absorption and rapid charge carrier separation. The nanostructures exhibit higher photocurrent and incident photon to electron conversion efficiency (IPCE) under no bias potential *versus* the Ag/AgCl electrode. We also analyzed the interface and photoelectrochemical characteristics of the nanostructure and revealed the kinetic process of the electron and hole transmission. In addition, the photoanode test shows the hydrogen production capability of the nanostructures from solar water splitting. These results verified that the ZnO and TiO_2 can be sensitized by the polymetallic sulfide for UV-Vis light driven energy conversion. Importantly, the approach we used to design the photoanode enables the development of micro-nano electronic devices with enhanced performance.

Introduction

Due to the growing global energy demand and increasing concerns on the energy-related environmental problems, solar energy, a sustainable and clean energy, has been considered as a potential energy source to tackle the energy and environmental issues.[1–8] Therefore, great efforts have been made to convert sunlight into usable energy effectively and economically. Photoelectrochemical (PEC) water splitting using solar illumination is proposed for the production of hydrogen fuel, because it is a simple and green process with high energy density.[9–12] Highly efficient and stable PEC systems have been employed for water splitting based on semiconductor materials, including TiO_2, Fe_2O_3, and ZnO.[13–18] Among them, a ZnO single-crystal nanorod array is one of the excellent candidates as the photoelectrode due to its great electron percolation pathways and light-harvesting ability.[19–21] On the other hand, anatase TiO_2 nanocrystals exposing the active facets[22–24] can be used to modify the surface of the individual ZnO single-crystal nanorod to improve the chemical stability of ZnO nanorods in an acidic or basic environment. More importantly, the surface modification of ZnO nanorods using TiO_2 nanocrystals can also enhance the surface activity *via* the compatible crystal lattice parameters and the band gap between ZnO and TiO_2.

However, both ZnO and TiO_2 are wide band gap semiconductors and they are only sensitive to UV light and exhibit fast recombination of the excitons which results in lower conversion efficiency of solar energy.[25–27] Metallic sulphide semiconductors with a narrow band gap have recently been employed to decorate the surface of ZnO nanowires for the extended visible light absorption, such as CdS, CdSe, and PbS.[28–34] The heterojunction interfaces of the oxides (TiO_2 or ZnO) and metallic sulphides can facilitate the separation and transportation of photogenerated charge carriers, thus improving the kinetics

[a]*CAS Key Laboratory of Bio-Medical Diagnostics, Suzhou Institute of Biomedical Engineering and Technology, Chinese Academy of Science (CAS), 88 Keling Road, Suzhou 215163, People's Republic of China. E-mail: wenfeidong@126.com*
[b]*Advanced Cytometry Labs, ARC Centre of Excellence for Nanoscale BioPhotonics (CNBP), Macquarie University, Sydney, NSW 2109, Australia*
[c]*Beijing Key Laboratory for Green Catalysis and Separation, Department of Chemistry and Chemical Engineering, Beijing University of Technology, Beijing 100124, People's Republic of China. E-mail: sunzc@ciomp.ac.cn*
[d]*Centre for Biomedical Materials and Engineering, Harbin Engineering University, Harbin 150001, China*

†Electronic supplementary information (ESI) available: More SEM and TEM images, XRD patterns, EDX spectra and hydrogen production data. See DOI: 10.1039/c5nr02127h

of water splitting processes to extend the lifetime of the charge.[27,35–37] However, the toxicity of Cd, Se, and Pb elements in the metallic sulphides is still a big concern. In addition, CdS quantum dots, possessing a relatively slower interfacial hole transfer rate compared to electron injection into metal oxides, cause hole-induced anodic corrosion.[38,39]

In this work, we proposed a new polymetallic sulphide solid-solution to decorate the hierarchical nanostructure of a co-axial ZnO@TiO_2 nanorod array as the photoelectrode for a solar driven PEC device. We characterized the sample morphology, crystal phase and elements. The optical absorption properties and interface properties were also analyzed. The mechanism of electron transmission kinetics of the novel hierarchical nanostructure was investigated. In addition, we performed the photoelectrochemical tests for the photovoltaic applications and concluded that the novel hierarchical nanostructure of the co-axial ZnO@TiO_2 nanorod array decorated with a polymetallic sulphide solid-solution is a promising multifunctional nanomaterial candidate for the micro-nano photoelectronic systems for biological sensing and medical detection.[40–42]

Results and discussion

The fabrication procedure of the hierarchical nanostructure of a co-axial ZnO@TiO_2 nanorod array decorated with a polymetallic sulfide solid-solution *via* hydrothermal synthesis is illustrated in Scheme 1. The fluorine-doped tin oxide (FTO) glass substrate spin-coated with ZnO seeds was put into a growth solution to obtain a ZnO nanorod array (ZnO NRA). Then TiO_2 was coated on each ZnO nanorod to form a ZnO@TiO_2 nanorod array (ZnO@TiO_2 NRA). Finally, a variety of nanorod array samples loaded with different amounts of polymetallic sulfide solid-solution on the surface were obtained. They were named from ZICS-1unit to ZICS-20unit according to the stoichiometry defined by the amount and concentration of the reaction mixture (see the Experimental section).

Morphology, structure and composition analysis

Fig. 1 shows the typical top-view and side-view of the ZnO NRA, ZnO@TiO_2 NRA and ZICS-15unit grown on FTO substrates using a field emission scanning electron microscope (FESEM). It can be seen from Fig. 1A and D that ZnO nanorods with a diameter of about 180 nm are perpendicularly aligned on the FTO substrate. The ZnO nanorod is in the shape of a hexagonal prism with even lateral surfaces. Due to fast axial direction growth, the top of ZnO nanorods is sharp (inset in Fig. 1A). Fig. 1B and C show the top-view images of ZnO@TiO_2 NRA and ZICS-15unit, respectively. It can be seen that the surface of ZnO@TiO_2 nanorods becomes rough and a nanostructured layer consisting of many unordered nanoparticles is formed. Some bright sphere nanoparticles and aggregates are irregularly distributed on the top and lateral surfaces of the ZICS-15unit. The nanorod diameters of ZnO@TiO_2 NRA and ZICS-15unit increase to about 200 nm. From the corresponding side-view images (Fig. 1E and F), it is also clearly shown that the TiO_2 nanoparticle layer wraps the ZnO nanorod, and the nanoparticles and aggregates are decorated

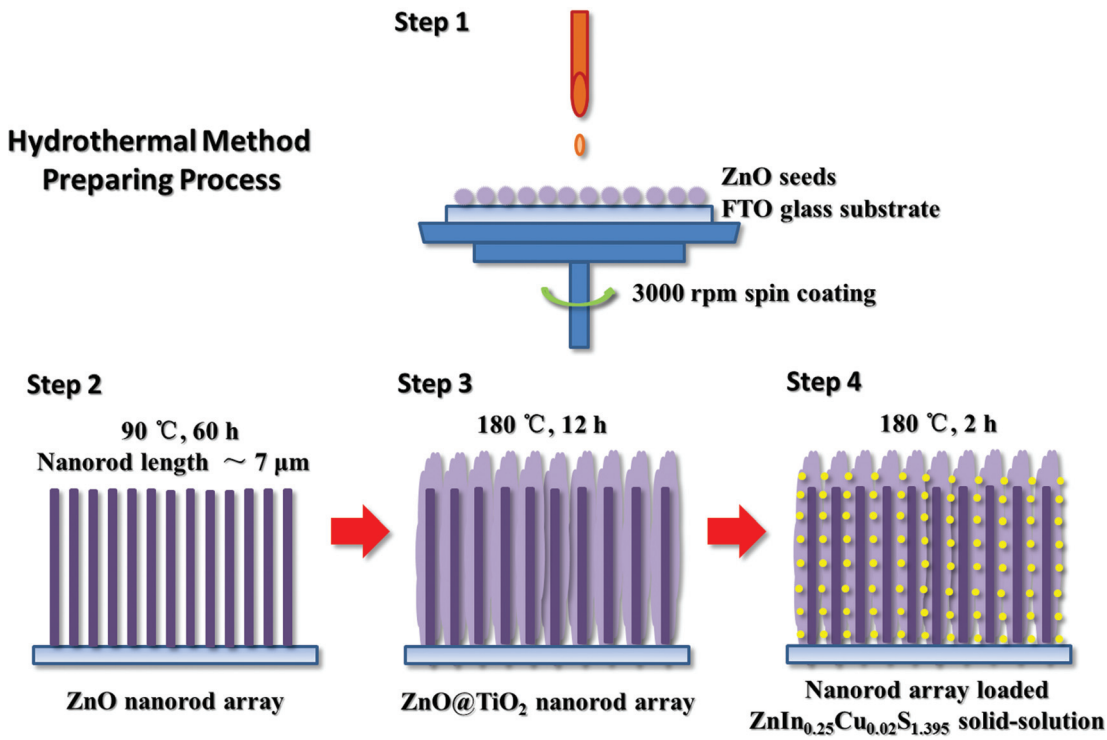

Scheme 1 Hydrothermal fabrication process of the ZnO@TiO_2 nanorod array film loaded with a polymetallic sulphide solid-solution.

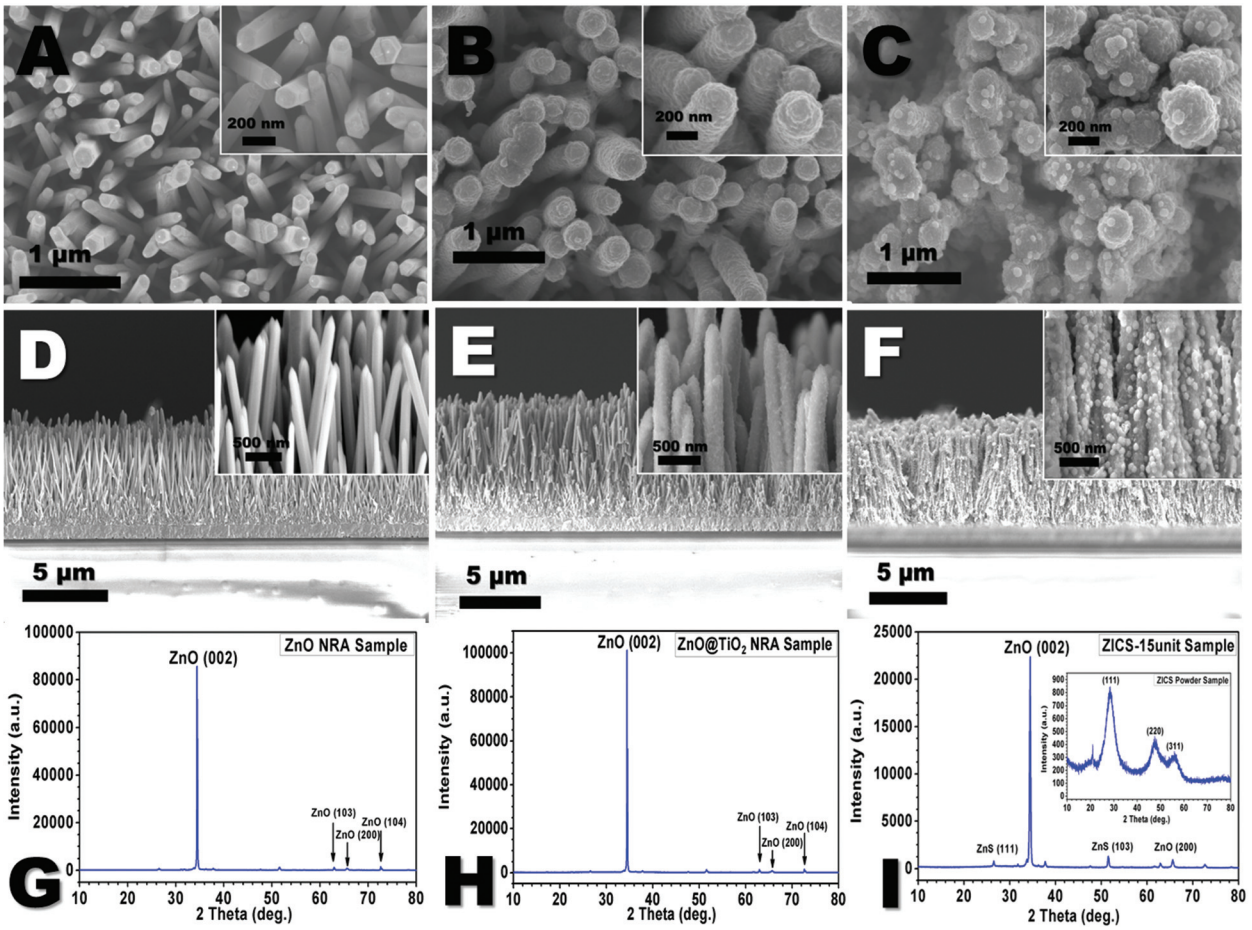

Fig. 1 Field emission scanning electron microscopy (FESEM) images of related samples. (A) Top-view of ZnO NRA, (B) top-view of ZnO@TiO_2 NRA, (C) top-view of the ZICS-15unit sample, (D), (E) and (F) are the side-views corresponding to (A), (B) and (C), respectively. All the insets shown are the corresponding magnified views. Meanwhile, the corresponding X-ray diffraction (XRD) patterns are shown as: (G) ZnO NRA, (H) ZnO@TiO_2 NRA, and (I) ZICS-15unit sample. The inset of (I) shows the XRD pattern of the ZICS powder sample as the reference.

onto the surface of the nanorod. The length of each ZnO nanorod is about 7 μm, which barely changes with the coating of TiO_2 and sulfides. The energy-dispersive X-ray spectroscopy (EDX) analysis shows that Zn and O, Zn, Ti and O, and Zn, Ti, Cu, In and S elements co-exist in the ZnO NRA, ZnO@TiO_2 NRA and ZICS-15unit samples, respectively (see Fig. S1 in the ESI†).

Fig. 1G–I show the X-ray diffraction (XRD) patterns of the ZnO NRA, ZnO@TiO_2 NRA and ZICS-15unit, respectively. The crystal structure of the ZICS powder, which is centrifugally collected from ZICS-15unit reaction liquid, is used as the reference (inset of Fig. 1I). A pronounced (002) diffraction peak of ZnO is shown in Fig. 1 due to the highly oriented ZnO nanorod array. The diffraction peak from other directions is relatively weak. It is hard to observe diffraction peaks of TiO_2 due to the small amount of TiO_2 on the ZnO nanorod surfaces. Trace amounts of ZnS diffraction peaks are observed from the ZICS-15unit sample. This could probably be attributed to the penetration of the sulfide through the TiO_2 layer and reaction with the ZnO nanorod in the hydrothermal environment. The XRD pattern of ZICS powder shows three broad peaks corresponding to (111), (220), and (311) of $ZnIn_{0.25}Cu_{0.02}S_{1.395}$, respectively.[43] With the increased amount of sulfide, the ZICS-20unit sample shows stronger ZnS diffraction peaks (see Fig. S2 in the ESI†), which is in good agreement with the lattice spacing of ZnS nanoparticles observed in high resolution transmission electron microscopy (TEM) images of the ZICS-20unit sample (see Fig. S4 in the ESI†). Based on the above results, we can conclude that the $ZnIn_{0.25}Cu_{0.02}S_{1.395}$ aggregates were successfully decorated onto the surfaces of the co-axial ZnO@TiO_2 nanorod array.

High resolution transmission electron microscopy (HRTEM) images and element mapping results of the ZICS-15unit sample are shown in Fig. 2. Fig. 2A reveals that the outside of the ZnO@TiO_2 nanorod consists of randomly-oriented hemisphere nanoparticles and aggregates with a size of 15–50 nm. The magnification of the selected partial nanorod area (Fig. 2B) reveals a layer of TiO_2 nanoparticles about 10 nm thick wrapping the surface of the ZnO nanorod. From Fig. 2C, the inner ZnO nanorod with unitary lattice

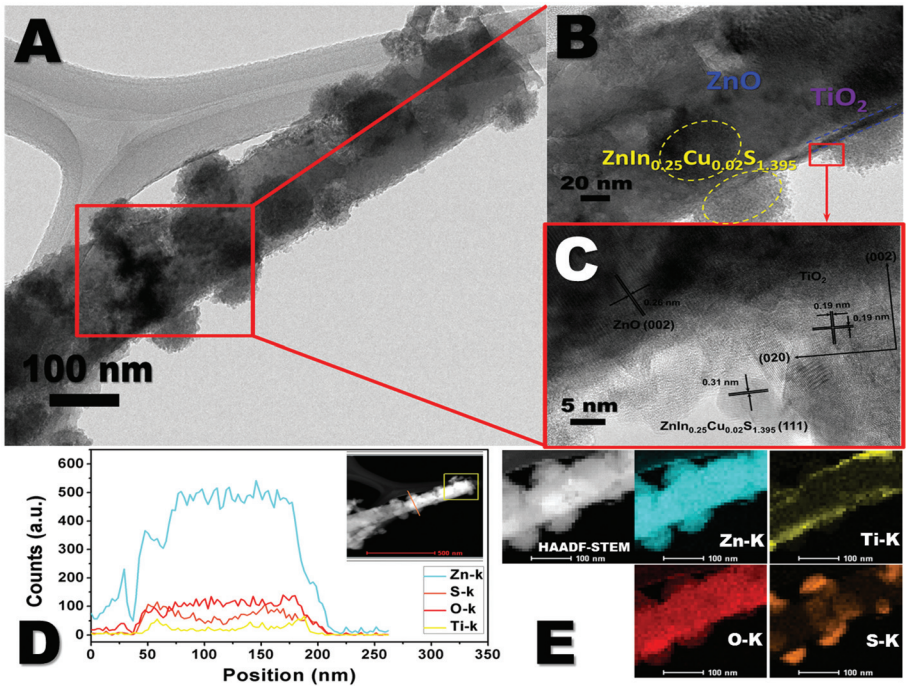

Fig. 2 (A) Transmission electron microscopy (TEM) image of the ZICS-15unit sample, (B) and (C) high resolution TEM (HRTEM) images of the selected square area shown in (A), (D) line scan profile of EDX spectra. It goes along the orange line crossing the nanorod as shown in the inset, which is a high angle annular dark-field scanning TEM (HAADF-STEM) image. The yellow square is the reference area for image signal processing, (E) elemental mapping of the ZICS-15unit sample.

fringes is a characteristic sign of the single-crystal structure, and the fringe spacing of 0.26 nm corresponds to the (002) plane of wurtzite type ZnO, which agree with the XRD patterns of related samples shown in Fig. 1. We can also find that the nanoparticle layer from the surface to the inside has a polycrystalline structure, and crystal grains have the fringe spacings of 0.19 nm and 0.31 nm, which match well with the interplanar spacings of the (002) plane of TiO_2 and the (111) plane of $ZnIn_{0.25}Cu_{0.02}S_{1.395}$, respectively.[18,22–24,43] Moreover, it is further verified that $ZnIn_{0.25}Cu_{0.02}S_{1.395}$ forms solid-solution rather than a compound mixture of ZnS, In_2S_3 and CuS due to its unitary fringe spacing and characteristic diffraction peak. Fig. 2D shows the line scan profile of the EDX spectra acquired along a line crossing the nanorod as shown in the inset (high angle annular dark-field scanning TEM (HAADF-STEM) image). The intensity of the curves provides evidence of the distribution density of all the elements indicating the core/layer structure. To confirm the multiple layer structure, elemental distribution mapping results are shown in Fig. 2E. The left STEM image shows the nanorod decorated with sulfide aggregates. The Zn element is well dispersed in whole nanorods and aggregates as both nanorods and aggregates contain Zn. In the Ti–K image, only the two edges of the nanorod show maxima, indicating that Ti only exists in the outer layer around the ZnO nanorod. In contrast, the O element is located on the position of the nanorod because O is mainly contributed from ZnO and TiO_2. On the aggregates, the O element signal obviously turns darker than that of the nanorod. Most of the S element is located on the aggregate site. These results clearly indicate that the TiO_2 nanoparticle layer wraps the ZnO nanorod well, and the polymetallic sulfide solid-solution forms nanoparticles and aggregates mingled onto the surface.

Absorption characterization

The optical absorption properties of the samples were tested. The UV-Vis absorption spectra and optical images of a series of nanorod array films on the FTO substrates are shown in Fig. 3. ZnO NRA and ZnO@TiO_2 NRA are white and show no absorption in the visible light range. Their absorption edges are below 400 nm in the UV light region. After loading the $ZnIn_{0.25}Cu_{0.02}S_{1.395}$ solid-solution, the nanorod array sample displayed colors from light yellow to dark brown with the increased amount of sulfide. The corresponding band edges of absorption spectra red-shift from 521 nm to 582 nm in the visible light region, that is to say, the corresponding bandgap varies from 2.39 eV to 2.14 eV by adjusting the loading amount of $ZnIn_{0.25}Cu_{0.02}S_{1.395}$ solid-solution while the absorption intensity also increases. However, an obvious absorption peak is observed in the UV-Vis spectrum of the ZICS-20unit sample, and the peak is probably due to the intensive scattering of small nanoparticles by loading excess $ZnIn_{0.25}Cu_{0.02}S_{1.395}$ solid-solution. In summary, it has been demonstrated that loading a $ZnIn_{0.25}Cu_{0.02}S_{1.395}$ solid-solution onto a co-axial

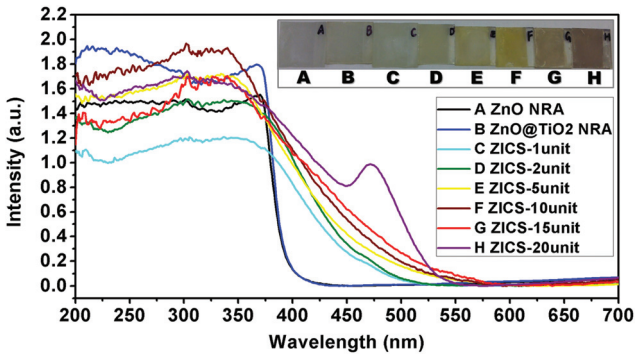

Fig. 3 UV-Vis absorption spectra of nanorod array film samples mentioned in this work. Insets show the optical images of the corresponding samples.

$ZnO@TiO_2$ nanorod array increases its absorption coefficient within a larger proportion of visible light to generate more photoinduced charge carriers.

Photoluminescence characterization

The photoluminescence spectra are shown in Fig. 4, and the kinetic mechanism of electron transmission and material interface properties of our samples was investigated. For 220 nm laser excitation (Fig. 4A), a ZnO intrinsic emission peak is at 400 nm, which increases with the loading amount of the sulphide. However, an intensity decrease was observed for the ZICS-20unit sample at 400 nm. It is probably because of the corrosion of the ZnO nanorod due to overloading of sulphide (see Fig. S3 in ESI†). The peaks located around 420 nm and 470 nm are attributed to the deep energy states caused by impurities of the ZnO nanorod, the broad spectra around 450 nm are assigned to the TiO_2 nanoparticle shell, and the broad baselines from 475 nm to 600 nm in the visible light region are brought about by loading a polymetallic sulphide solid-solution. The ZICS powder has no evident emission peaks in this region under the same excitation. Furthermore, when 450 nm laser excitation was applied (Fig. 4B), the peak around 550 nm of the ZICS powder, intrinsic emission of polymetallic sulphide solid-solution, gradually disappeared with sulphide addition. By comparison with different laser excitations, we can infer the existence of electron transfer between core/layer interfaces under solar UV-Vis light illumination. First, both the inner ZnO nanorod and the outer layer including TiO_2 and polymetallic sulfide solid-solution are excited with UV light, so the electron transfer from sulphide to ZnO leads to strengthening of the intrinsic emission of ZnO. Second, only the $ZnIn_{0.25}Cu_{0.02}S_{1.395}$ solid-solution can absorb the visible light and rapidly carry the excited electrons to ZnO through stepwise energy level arrangements. Then the inner ZnO nanorod acts as a good electron transport channel to achieve fast separation of photoinduced electrons and holes in working circuits.

Photoelectrochemical measurements

Fig. 5A shows the *J–V* characteristics and current–time transient responses of these samples to evaluate their photoelectrochemical activity. Linear sweep voltammograms (LSV) are operated both in the dark and under visible light irradiation. In the dark, all electrodes show tiny currents without any difference. Therefore, only the current curve of the ZnO NRA electrode is illustrated as a dashed line in Fig. 5A. Under visible light illumination shown in Fig. 5A, the ZnO NRA and $ZnO@TiO_2$ NRA electrode exhibit very low photocurrent, whereas the photocurrents of the samples loaded with sulfide are obviously enhanced within the entire scanning region. The photocurrent density gradually increases with the increment of the sulfide loading amount, because the $ZnIn_{0.25}Cu_{0.02}S_{1.395}$ solid-solution is a visible light absorber and more sulfide can convert the more visible light into current. At an applied potential of 0 V *versus* Ag/AgCl, the current densities of ZnO NRA and $ZnO@TiO_2$ NRA are −0.32 and −0.37 mA cm^{-2}, respectively. Under the same conditions, the current densities of the ZICS-1unit, ZICS-2unit, ZICS-5unit, ZICS-10unit, ZICS-15unit and ZICS-20unit are −1.27, −2.89, −4.21, −5.56, −7.39, and −5.23 mA cm^{-2}, respectively. Moreover, the onset potentials of the ZnO NRA and $ZnO@TiO_2$ NRA films are around −0.25 and −0.27 V, and the value shifts from −0.33 to −0.56 V after $ZnIn_{0.25}Cu_{0.02}S_{1.395}$ solid-solution is loaded. The

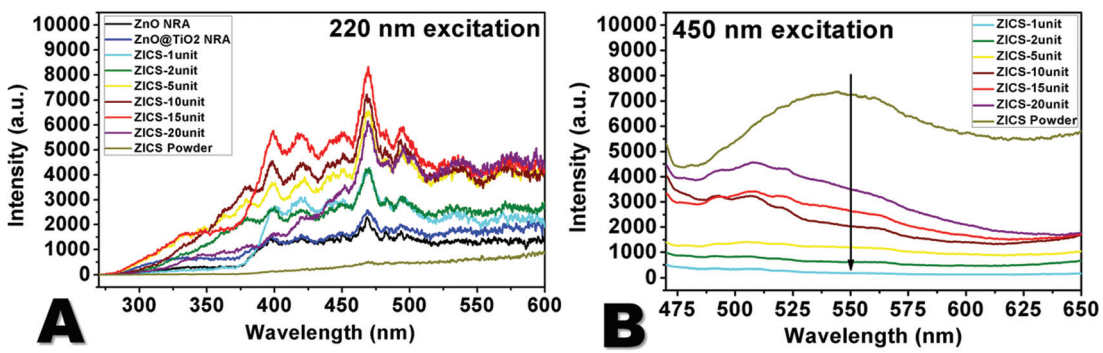

Fig. 4 Photoluminescence spectra of nanorod array film samples mentioned in this work. (A) Emission spectra under 220 nm laser excitation, and (B) emission spectra under 450 nm laser excitation.

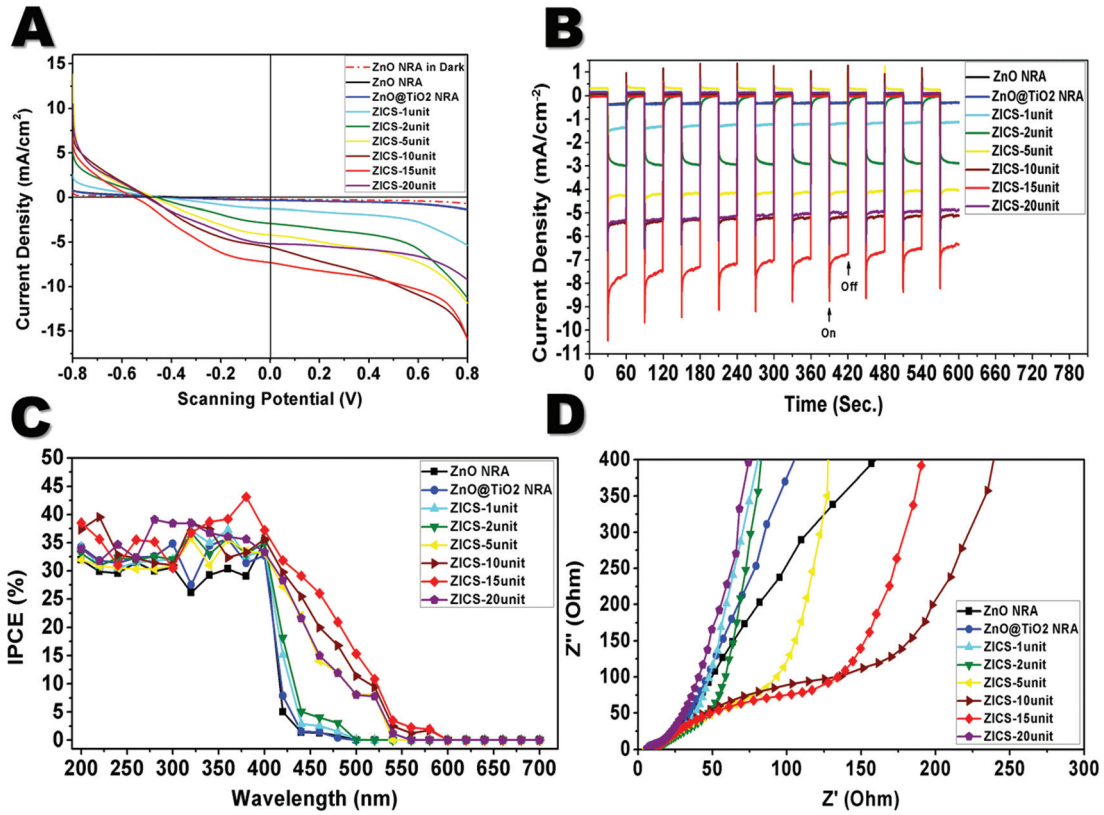

Fig. 5 Photoelectrochemical measurements. (A) Current–potential curves of the corresponding samples in a 0.5 mol L^{-1} Na_2SO_4 solution. Scan rate: 100 mV s^{-1}, (B) *I–T* curves of the corresponding samples in a 0.5 mol L^{-1} Na_2SO_4 solution, applied potential 0 V *versus* Ag/AgCl with a UV light cut-off filter (λ > 400 nm), (C) IPCE profiles of the corresponding samples collected at 0 V *versus* Ag/AgCl, AC amplitude: 5 mV, frequency range: 100 kHz–1 Hz, (D) electrochemical impedance spectra (EIS, Nyquist plots) of the corresponding samples at 0 V *versus* Ag/AgCl.

negative shift of the onset potential indicates the decreased surface state densities of the electrodes and increased charge transfer rates at the interfaces.[44,45]

The visible light responses of the samples with a UV light cut-off filter (λ > 400 nm) at an applied potential of 0 V *versus* Ag/AgCl are shown in Fig. 5B. A higher photocurrent corresponds to a higher efficiency of hydrogen evolution of the PEC device. When the light is turned on, the photocurrent reaches a peak value and gradually decays to a steady state. A longer decay time is associated with a longer lifetime of photogenerated charge carriers.[46] The current densities of the ZnO NRA and ZnO@TiO_2 NRA electrodes are 0.31 and 0.34 mA cm^{-2}, respectively. The current density of the ZnO@TiO_2 NRA with a $ZnIn_{0.25}Cu_{0.02}S_{1.395}$ solid-solution increases from 1.25 to 7.28 mA cm^{-2}, which is about 4 to 24 times more than that of the ZnO NRA sample. However, the ZnO NRA corrosion of the ZICS-20unit sample causes the decline of the photoelectrochemical performance compared with the other samples as mentioned above.

To quantify the photoelectrochemical response of the samples to incident light with various wavelengths, the IPCE measurements were performed on the sample electrodes at 0 V *versus* Ag/AgCl (Fig. 5C). The photoresponse of the ZnO NRA and ZnO@TiO_2 NRA are only active in the UV region. With the $ZnIn_{0.25}Cu_{0.02}S_{1.395}$ solid-solution loaded onto the ZnO@TiO_2 NRA, the photoresponse of the sample electrodes extends to the wavelength at 580 nm, which agrees with the absorption edge of $ZnIn_{0.25}Cu_{0.02}S_{1.395}$ solid-solution (Fig. 3). With the increased polymetallic sulphide amount the series of ZICS samples exhibit both extended coverage of photoresponse and increased IPCE values in the visible light region. The ZICS-15unit electrode exhibits a maximum IPCE of approximately 43.2% at 380 nm, and then 31.8% at 420 nm, 29.3% at 440 nm, 26.2% at 460 nm and 20.5% at 480 nm, respectively. The improvement is mainly attributed to the PN heterojunctions formed between the co-axial ZnO@TiO_2 nanorod and polymetallic sulphide solid-solution on its surfaces. The ZnS nanoparticles in the ZICS-20unit sample cause the photoresponse drop dramatically due to the damage of interface contact from corrosion. In addition, we believe that the lower IPCE in the visible light region compared to the UV light region is due to mismatched band alignments of the ZnO@TiO_2 nanorod and $ZnIn_{0.25}Cu_{0.02}S_{1.395}$ solid-solution to some extent.

Electrochemical impedance spectroscopy (EIS, which are Nyquist plots here) was carried out to interpret the photocurrent change and the photon conversion efficiency of the samples. Fig. 5D shows electrochemical impedance spectra of

nanorod arrays at AC frequency from 100 kHz to 1 Hz, which was performed under simulated solar illumination at open circuit voltage. Considering the molecular polarization caused by high frequency alternating-electric field, the charge transfer resistance (R_{ct}) from the photoelectrodes to redox species in the electrolyte can be calculated by fitting the semi-arc in the low frequency region. A smaller radius represents lower electron transport resistance and higher separation efficiency of the photogenerated electrons and holes. From Fig. 5D, we can deduce that the R_{ct} of the loaded $ZnIn_{0.25}Cu_{0.02}S_{1.395}$ solid-solution film is smaller than that of ZnO NRA and ZnO@TiO_2 NRA films, which explains the better photoresponse as shown in Fig. 5B. It indicates that the formed PN heterojunctions between $ZnIn_{0.25}Cu_{0.02}S_{1.395}$ solid-solution and ZnO@TiO_2 NRA establish an internal electrostatic field to promote the transportation of charge carriers and restrain the recombination of electrons and holes, so more charge carriers take part in the redox reactions. Again, the corrosion of the ZICS-20unit sample passivates the electron transmission in ZnO single-crystals by the appearance of ZnS nanoparticles. Thus, its R_{ct} becomes larger than that of ZnO NRA and ZnO@TiO_2 NRA samples.

Photocatalysis and hydrogen production

Scheme 2 illustrates the photoinduced electron separation and transportation process in the ZnO@TiO_2 NRA loaded $ZnIn_{0.25}Cu_{0.02}S_{1.395}$ solid-solution. ZnO nanorods play the role of an effective percolation pathway for the transportation of electrons from the $ZnIn_{0.25}Cu_{0.02}S_{1.395}$ solid-solution to inner nanorods. TiO_2, as an activated layer, has a high surface-to-volume ratio for more photocatalysis reactive sites, and enhances the photocatalysis activity by exposing the active (001) plane and protecting ZnO from harsh environments. The coarse surface of ZnO@TiO_2 nanorods reduces the reflection of incident light so as to increase the harvesting of incident light. $ZnIn_{0.25}Cu_{0.02}S_{1.395}$ solid-solution with a direct narrow band gap and a high absorption coefficient can be employed as the visible light absorber to generate photoinduced charge carriers.

Under UV-Vis light illumination, photogenerated electrons in the conduction band of sulphide flow to that of ZnO and TiO_2, and further to the counter electrode through the external circuit to produce hydrogen. A stepwise conduction band edge limits the electron flux and reduces the recombination of the electrons and the holes, leading to enhancement in the photovoltaic performance. Then it significantly enhances the photocurrent density and conversion efficiency of the material. Furthermore, we also used the ZICS-15unit film sample for hydrogen production, and we received about 12 μmol hydrogen gas during the 4 h reaction (Fig. 6). Although the hydrogen gas produced within this sample system is much lower than that produced within the traditional mesoporous powder materials (*e.g.* commercial TiO_2 P25 powder), it is still an acceptable result considering the lower amount of uncontrollable stoichiometric loaded material due to the nanorod array film under liquid reaction conditions. Simultaneously, photogenerated holes in the valence band of the ZnO and TiO_2 are transferred to sulphide, which reacts with the hole scavengers S^{2-} and SO_3^{2-} adhering to the sulphide surface.

A uniform semiconductor core/layer nanostructure with an effective heterojunction like this combines the merits of all components and meets the requirements of large light absorp-

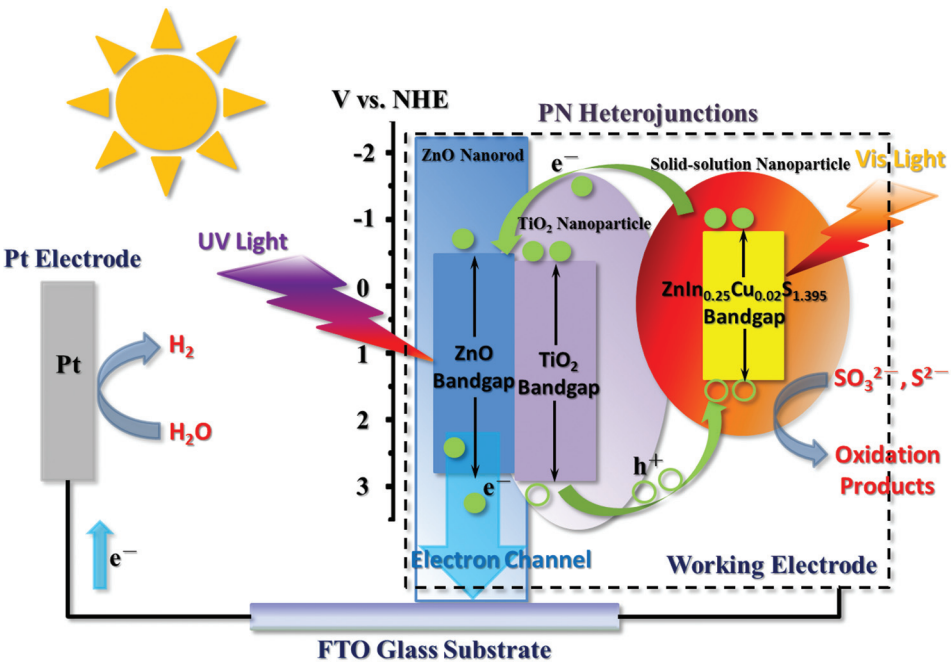

Scheme 2 Photoinduced electron separation and transportation process in the ZnO@TiO_2 nanorod array film loaded with a $ZnIn_{0.25}Cu_{0.02}S_{1.395}$ solid-solution.

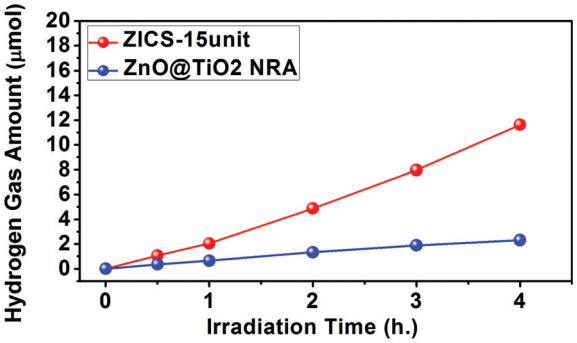

Fig. 6 Amount of H_2 evolution according to the reaction time for one ZICS-15unit sample and one ZnO@TiO_2 NRA sample, respectively. The 350 mL reaction vessel contains 1.0 mol L^{-1} Na_2SO_3 and 1.0 mol L^{-1} Na_2S stirring aqueous solution as electron donors.

tion, rapid separation of charge carriers and reduction of the surface defects of nanorods. In addition, a nanorod array film also has a higher surface area and can be suitably integrated into micro-nano electronic systems.

Conclusions

A ZnO@TiO_2 core/layer nanorod array sensitized with $ZnIn_{0.25}Cu_{0.02}S_{1.395}$ solid-solution nanoparticles was fabricated *via* a facile hydrothermal process. The photocurrent of the heteronanostructure reached 7.28 mA cm^{-2}, and its IPCE was significantly enhanced in the visible light region. In such a combined nanostructure, ZnO acts as a framework and pathway for electron transport and the $ZnIn_{0.25}Cu_{0.02}S_{1.395}$ solid-solution can capture a large proportion of visible light due to its high absorption coefficient and a narrow direct bandgap. TiO_2 plays the role of a protective layer for ZnO and enlarges the surface area of photocatalysis. Moreover, the ZnO nanorod with the TiO_2 layer wrapped outside and the polymetallic sulphide solid-solution decorated on surfaces together form an intimate PN heterostructure between interfaces, which accelerates charge injection from one semiconductor to another. It leads to efficient photoexcited charge separation and reduction of the recombination of electron–hole pairs by the internal electrostatic field in the interface. The above factors are supposed to be the main reasons for the enhanced photoelectrical response of our material system. We have also demonstrated its great potential in integrated photoelectric devices and solar photocatalysis water splitting.

Experimental section

Preparation of ultralong ZnO nanorod arrays

To obtain ultralong ZnO nanorod arrays, we used polyethyleneimine (PEI) to suppress the homogeneous nucleation during the ZnO nanorod growth process. Then the polymer chain of PEI was preferentially adsorbed onto certain crystal faces of ZnO clusters, which initially formed due to thermal fluctuation and are small, and inhibit further crystal growth along these faces to develop the ZnO bulk. As a result, growth of ZnO nanorods can normally occur on the seeded substrates at a reasonably high growth rate.

In a typical modified route,[47,48] the zinc acetate dehydrate and ethanolamine are mixed in a 1 : 1.2 molar ratio in 25 mL 2-methoxyethanol to ensure the concentration of $Zn(CH_3COO)_2$ as 0.2 mol L^{-1}. The above solution is stirred at 60 °C for 30 min and then spin-coated (3000 rpm for 1 min) on FTO glass substrates, which are ultrasonically cleaned by acetone, ethanol and deionized water in this order. Next, we put the pretreated FTO glass substrates in an electric oven at 400 °C for 2 h to get ZnO grains.

To prepare the ZnO nanorod array growth solution, zinc nitrate hexahydrate and hexamethylenetetramine (HMTA) are digested in 100 mL deionized water to maintain the concentration of $Zn(NO_3)_2$ at 25 mmol L^{-1} and the molar ratio of $Zn(NO_3)_2$: HMTA at 1 : 1. The concentration of PEI is set at 0.005 mol L^{-1} in our work. A ZnO nanorod array is grown on the FTO substrate with ZnO grains by soaking in the above solution at 90 °C for 12 h. Then fresh growth solution is used to repeat the above procedure five times to obtain ultralong nanorod arrays, and the total actual growth time is more than 60 h in our experiments.

Preparation of ZnO@TiO_2 core/layer nanorod array films

The FTO substrate with a ZnO nanorod film is put into a Teflon lined stainless steel autoclave, which contains 7.5 μL diethylenetriamine (DETA), 10.5 mL isopropyl alcohol (AR grade, Beijing Chemical Works) and 50–70 μL titanium(IV) isopropoxide. The sealed autoclave is heated up to 180 °C for 12 h in an electric oven. Following this reaction the autoclave is naturally cooled down to room temperature. The as-prepared samples are gently rinsed with ethanol and acetone and dried at room temperature. Finally, the samples are annealed at 400 °C for 2 h to reinforce the crystal phase of TiO_2.

Preparation of ZnO@TiO_2 films loaded with Zn–In–Cu–S solid-solution

The Zn–In–Cu–S solid-solution is loaded *via* the solvothermal method. In a typical experiment, $Zn(CH_3COO)_2{\cdot}2H_2O$ (0.03 mmol), $InCl_3{\cdot}4H_2O$ (0.005 mmol), and thiourea (0.0385 mmol) were dissolved into 8 mL of ethylene glycol using a magnetic stirrer to form a clear solution. We also prepared 0.2 mL of 0.005 mol L^{-1} $Cu(CH_3COO)_2{\cdot}H_2O$/ethylene glycol solution to add dropwise into the above solution under constant stirring. The above amount and concentration of the reaction mixture can be defined as a unit dose (named ZICS-1unit), and we increase the stoichiometry with respect to the ZICS-1unit to obtain ZICS-2unit (twice), ZICS-5unit (five times) and so on, which are named as mentioned above. The as-prepared solution is immediately transferred into an autoclave (Teflon cups with 15 mL inner volume), and the FTO substrate with a ZnO@TiO_2 nanorod array film is maintained in the Teflon cup at 180 °C for 2 h and then air-cooled to room temp-

erature. The FTO substrate is washed several times with absolute ethanol and finally air dried.

Material morphology and characterization

Morphology and elemental chemical composition analyses of the nanoarray photoelectrode are carried out using field emission scanning electron microscope (FESEM) JEOL JSM 4800F combined with energy-dispersive X-ray spectroscopy (EDX). The crystallographic and detailed microscopic structure analyses are observed by high resolution transmission electron microscopy (HRTEM) on FEI Tecnai F20 operated at 200 kV, equipped with a line scan profile of EDX and elemental mappings. X-ray diffraction (XRD) patterns are recorded on a Rigaku D/Max-2000 diffractometer with Cu Kα radiation (λ = 0.15406 nm). UV-Vis spectra to analyze the band gap structure are measured by a Shimadzu UV-3600 UV-Vis-NIR scanning spectrophotometer using $BaSO_4$ as a reference. A Hitachi F7000 UV-Vis spectrophotometer equipped with a Xe lamp source is employed to determine the photoluminescence spectra of our samples under different excitations.

Photoelectrochemical measurements

In our experiments, a three-electrode configuration in a quartz cell is assembled to test the photoelectrochemical activity of the samples on a Chenghua electrochemical workstation (CHI660C, Shanghai). A Pt plate and a commercially available Ag/AgCl electrode are used as the counter and reference electrodes, and the prepared samples are employed as working electrodes. The effective surface area of the working electrode is 0.5 × 0.5 cm^2. All measured potential values are against an Ag/AgCl reference electrode unless otherwise indicated. The electrolyte used in all measurements is an aqueous solution containing 0.5 mol L^{-1} Na_2SO_4. A 300 W xenon lamp (PLS-SXE300/300UV) equipped with a UV-light cut-off filter (λ > 400 nm) is used as a visible light irradiation source, and its light intensity is 100 mW cm^{-2}. The linear sweep voltammograms (LSV) are obtained at 100 mV s^{-1} in a potential range of −0.8 V to +0.8 V *versus* Ag/AgCl both in the dark and under illumination. The chronoamperometry curves (*I–T* curve) of the films are obtained at 0 V *versus* Ag/AgCl. Electrochemical impedance spectroscopy (EIS) is performed under illumination with an AC amplitude of 5 mV and frequency range between 100 kHz and 1 Hz. The PLS-SXE300/300UV xenon lamp and a monochromator (Monochromator 300, Changtuo Technology Co., Ltd.) are used to measure wavelength-dependent photocurrents of all samples. The monochromatic light intensity is measured with a radiometer for subsequent calculations. The incident photon to electron conversion efficiency (IPCE) of the samples is calculated as follows:

$$\mathrm{IPCE} = 1240I(\mathrm{mA\ cm^{-2}})/[\lambda(\mathrm{nm})J_{\mathrm{light}}\ (\mathrm{mW\ cm^{-2}})]$$

where I is the photocurrent density, λ is the wavelength of the monochromatic light, and J_{light} is the monochromatic light intensity.

Photocatalytic hydrogen production

The production is performed in a closed gas-circulation photoelectrochemical system with a side window, and we use one ZICS-15unit sample in a 350 mL stirring aqueous solution containing 1.0 mol L^{-1} Na_2SO_3 and 1.0 mol L^{-1} Na_2S as electron donors for hydrogen production. The reaction without Pt material catalysis is carried out for 4 h by irradiating the mixture with light from a 300 W Xe lamp, which is equipped with an optical filter (λ > 400 nm) to cut off the light in the UV region. The amount of the produced hydrogen gas was measured by gas chromatography (Agilent 6820) with a thermal conductivity detector (TCD) and argon as the carrier gas.

Conflict of interest

The authors declare no competing financial interest.

Acknowledgements

This work was supported by the National Natural Science Foundation of China (No. 61306081 61176016 and 51201045, the National Basic Research Program of China (No. 2013CB933900 and 2014CB931800), the Science and Technology Department of Jilin Province (No. 20130522142JH, 20121801) and the Science and Technology Department of Suzhou City (No. ZXY201434). We acknowledge the support of the "Hundred Talent Program" of CAS.

References

1 A. Fujishima and K. Honda, Electrochemical photolysis of water at a semiconductor electrode, *Nature*, 1972, **238**, 37–38.
2 A. J. Nozik and J. R. Miller, Introduction to Solar Photon Conversion, *Chem. Rev.*, 2010, **110**, 6443–6445.
3 T. R. Cook, D. K. Dogutan, S. Y. Reece, Y. Surendranath, T. S. Teets and D. G. Nocera, Solar Energy Supply and Storage for the Legacy and Nonlegacy Worlds, *Chem. Rev.*, 2010, **110**, 6474–6502.
4 A. Kubacka, M. Fernandez-Garcia and G. Colon, Advanced Nanoarchitectures for Solar Photocatalytic Applications, *Chem. Rev.*, 2012, **112**, 1555–1614.
5 N. S. Lewis and D. G. Nocera, Powering the planet: Chemical challenges in solar energy utilization, *Proc. Natl. Acad. Sci. U. S. A.*, 2006, **103**, 15729–15735.
6 J. Barber, Biological solar energy, *Philos. Trans. R. Soc. London A*, 2007, **365**, 1007–1023.
7 Y.-H. Su, Y.-F. Ke, S.-L. Cai and Q.-Y. Yao, Surface plasmon resonance of layer-by-layer gold nanoparticles induced photoelectric current in environmentally-friendly plasmon-sensitized solar cell, *Light: Sci. Appl.*, 2012, **1**, e14, DOI: 10.1038/lsa.2012.14.

8 E. D. Kosten, J. H. Atwater, J. Parsons, A. Polman and H. A. Atwater, Highly efficient GaAs solar cells by limiting light emission angle, *Light: Sci. Appl.*, 2013, **2**, e45, DOI: 10.1038/lsa.2013.1.

9 A. J. Bard and M. A. Fox, Artificial Photosynthesis: Solar Splitting of Water to Hydrogen and Oxygen, *Acc. Chem. Res.*, 1995, **28**, 141–145.

10 Y. Tachibana, L. Vayssieres and J. R. Durrant, Artificial photosynthesis for solar water-splitting, *Nat. Photonics*, 2012, **6**, 511–518.

11 R. M. Navarro, M. C. Alvarez-Galvan, J. A. Villoria de la Mano, S. M. Al-Zahrani and J. L. G. Fierro, A framework for visible-light water splitting, *Energy Environ. Sci.*, 2010, **3**, 1865–1882.

12 F. E. Osterloh, Inorganic nanostructures for photoelectrochemical and photocatalytic water splitting, *Chem. Soc. Rev.*, 2013, **42**, 2294–2320.

13 X. Chen, L. Liu, P. Y. Yu and S. S. Mao, Increasing Solar Absorption for Photocatalysis with Black Hydrogenated Titanium Dioxide Nanocrystals, *Science*, 2011, **331**, 746–750.

14 M. Murdoch, G. I. N. Waterhouse, M. A. Nadeem, J. B. Metson, M. A. Keane, R. F. Howe, J. Llorca and H. Idriss, The effect of gold loading and particle size on photocatalytic hydrogen production from ethanol over Au/TiO_2 nanoparticles, *Nat. Chem.*, 2011, **3**, 489–492.

15 G. Wang, H. Wang, Y. Ling, Y. Tang, X. Yang, R. C. Fitzmorris, C. Wang, J. Z. Zhang and Y. Li, Hydrogen-Treated TiO_2 Nanowire Arrays for Photoelectrochemical Water Splitting, *Nano Lett.*, 2011, **11**, 3026–3033.

16 C. Y. Cummings, F. Marken, L. M. Peter, K. G. Upul Wijayantha and A. A. Tahir, New Insights into Water Splitting at Mesoporous α-Fe_2O_3 Films: A Study by Modulated Transmittance and Impedance Spectroscopies, *J. Am. Chem. Soc.*, 2012, **134**, 1228–1234.

17 B. Klahr, S. Gimenez, F. Fabregat-Santiago, J. Bisquert and T. W. Hamann, Photoelectrochemical and Impedance Spectroscopic Investigation of Water Oxidation with "Co-Pi"-Coated Hematite Electrodes, *J. Am. Chem. Soc.*, 2012, **134**, 16693–16700.

18 A. Kudo and Y. Miseki, Heterogeneous photocatalyst materials for water splitting, *Chem. Soc. Rev.*, 2009, **38**, 253–278.

19 C. Klingshirn, ZnO: Material, Physics and Applications, *ChemPhysChem*, 2007, **8**, 782–803.

20 Y. Bai, H. Yu, Z. Li, R. Amal, G. Q. Lu and L. Wang, In Situ Growth of a ZnO Nanowire Network within a TiO_2 Nanoparticle Film for Enhanced Dye-Sensitized Solar Cell Performance, *Adv. Mater.*, 2012, **24**, 5850–5856.

21 S. Chu, G. Wang, W. Zhou, Y. Lin, L. Chernyak, J. Zhao, J. Kong, L. Li, J. Ren and J. Liu, Electrically pumped waveguide lasing from ZnO nanowires, *Nat. Nanotechnol.*, 2011, **8**, 506–510.

22 H. G. Yang, G. Liu, S. Z. Qiao, C. H. Sun, Y. G. Jin, S. C. Smith, J. Zou, H. M. Cheng and G. Q. Lu, Solvothermal Synthesis and Photoreactivity of Anatase TiO_2 Nanosheets with Dominant {001} Facets, *J. Am. Chem. Soc.*, 2009, **131**, 4078–4083.

23 Y. Dai, C. M. Cobley, J. Zeng, Y. Sun and Y. Xia, Synthesis of Anatase TiO_2 Nanocrystals with Exposed {001} Facets, *Nano Lett.*, 2009, **9**, 2455–2459.

24 W. Q. Fang, X.-Q. Gong and H. G. Yang, On the Unusual Properties of Anatase TiO_2 Exposed by Highly Reactive Facets, *J. Phys. Chem. Lett.*, 2011, **2**, 725–734.

25 S. Panigrahi and D. Basak, Core–shell TiO_2@ZnO nanorods for efficient ultraviolet photodetection, *Nanoscale*, 2011, **3**, 2336–2341.

26 X. Yan, C. Zou, X. Gao and W. Gao, ZnO/TiO_2 core-brush nanostructure: processing, microstructure and enhanced photocatalytic activity, *J. Mater. Chem.*, 2012, **22**, 5629–5640.

27 S. G. Kumar and L. G. Devi, Review on Modified TiO_2 Photocatalysis under UV/Visible Light: Selected Results and Related Mechanisms on Interfacial Charge Carrier Transfer Dynamics, *J. Phys. Chem. A*, 2011, **115**, 13211–13241.

28 Y.-X. Yu, W.-X. Ouyang, Z.-T. Liao, B.-B. Du and W.-D. Zhang, Construction of ZnO/ZnS/CdS/$CuInS_2$ Core–Shell Nanowire Arrays via Ion Exchange: p-n Junction Photoanode with Enhanced Photoelectrochemical Activity under Visible Light, *ACS Appl. Mater. Interfaces*, 2014, **6**, 8467–8474.

29 J. Xu, X. Yang, H. Wang, X. Chen, C. Luan, Z. Xu, Z. Lu, V. A. L. Roy, W. Zhang and C.-S. Lee, Arrays of ZnO/$Zn_xCd_{1-x}Se$ Nanocables: Band Gap Engineering and Photovoltaic Applications, *Nano Lett.*, 2011, **11**, 4138–4143.

30 W. Sheng, B. Sun, T. Shi, X. Tan, Z. Peng and G. Liao, Quantum Dot-Sensitized Hierarchical Micro/Nanowire Architecture for Photoelectrochemical Water Splitting, *ACS Nano*, 2014, **8**, 7163–7169.

31 M. Seol, E. Ramasamy, J. Lee and K. Yong, Highly Efficient and Durable Quantum Dot Sensitized ZnO Nanowire Solar Cell Using Noble-Metal-Free Counter Electrode, *J. Phys. Chem. C*, 2011, **115**, 22018–22024.

32 J. Xu, C.-Y. Luan, Y.-B. Tang, X. Chen, J. A. Zapien, W.-J. Zhang, H.-L. Kwong, X.-M. Meng, S.-T. Lee and C.-S. Lee, Low-Temperature Synthesis of $CuInSe_2$ Nanotube Array on Conducting Glass Substrates for Solar Cell Application, *ACS Nano*, 2010, **4**, 6064–6070.

33 J. Jean, S. Chang, P. R. Brown, J. J. Cheng, P. H. Rekemeyer, M. G. Bawendi, S. Gradecak2 and V. Bulovic, ZnO Nanowire Arrays for Enhanced Photocurrent in PbS Quantum Dot Solar Cells, *Adv. Mater.*, 2013, **25**, 2790–2796.

34 J. Gao, J. M. Luther, O. E. Semonin, R. J. Ellingson, A. J. Nozik and M. C. Beard, Quantum Dot Size Dependent *J-V* Characteristics in Heterojunction ZnO/PbS Quantum Dot Solar Cells, *Nano Lett.*, 2011, **11**, 1002–1008.

35 B. D. Yuhas and P. Yang, Nanowire-Based All-Oxide Solar Cells, *J. Am. Chem. Soc.*, 2009, **131**, 3756–3761.

36 H. Tada, T. Mitsui, T. Kiyonaga, T. Akita and K. Tanaka, All-solid-state Z-scheme in CdS-Au-TiO_2 three-component nanojunction system, *Nat. Mater.*, 2006, **5**, 782–786.

37 D. Chen, H. Zhang, S. Hu and J. Li, Preparation and Enhanced Photoelectrochemical Performance of Coupled Bicomponent ZnO-TiO_2 Nanocomposites, *J. Phys. Chem. C*, 2008, **112**, 117–122.

38 A. J. Nozik, M. C. Beard, J. M. Luther, M. Law, R. J. Ellingson and J. C. Johnson, Semiconductor Quantum Dots and Quantum Dot Arrays and Applications of Multiple Exciton Generation to Third-Generation Photovoltaic Solar Cells, *Chem. Rev.*, 2010, **110**, 6873–6890.

39 L. Ge, F. Zuo, J. Liu, Q. Ma, C. Wang, D. Sun, L. Bartels and P. Feng, Synthesis and Efficient Visible Light Photocatalytic Hydrogen Evolution of Polymeric g-C_3N_4 Coupled with CdS Quantum Dots, *J. Phys. Chem. C*, 2012, **116**, 13708–13714.

40 A. Menzel, K. Subannajui, F. Güder, D. Moser, O. Paul and M. Zacharias, Multifunctional ZnO-Nanowire-Based Sensor, *Adv. Funct. Mater.*, 2011, **21**, 4342–4348.

41 S.-Y. Lin, S.-J. Chang and T.-J. Hsueh, ZnO nanowires modified with Au nanoparticles for nonenzymatic amperometric sensing of glucose, *Appl. Phys. Lett.*, 2014, **104**, 193704.

42 R. Yu, C. Pan and Z. L. Wang, High performance of ZnO nanowire protein sensors enhanced by the piezoelectronic effect, *Energy Environ. Sci.*, 2013, **6**, 494–499.

43 Y. Li, G. Chen, Q. Wang, X. Wang, A. Zhou and Z. Shen, Hierarchical ZnS-In_2S_3-CuS Nanospheres with Nanoporous Structure: Facile Synthesis, Growth Mechanism, and Excellent Photocatalytic Activity, *Adv. Funct. Mater.*, 2010, **20**, 3390–3398.

44 K. H. Yoon, C. W. Shin and D. H. Kang, Photoelectrochemical Conversion in a WO_3 Coated p-Si Photoelectrode: Effect of Annealing Temperature, *J. Appl. Phys.*, 1997, **81**, 7024–7029.

45 K. H. Yoon, D. K. Seo, Y. S. Cho and D. H. Kang, Effect of Pt Layers on the Photoelectrochemical Properties of a WO_3/p-Si Electrode, *J. Appl. Phys.*, 1998, **84**, 3954–3959.

46 G. P. Dai, J. G. Yu and G. Liu, Synthesis and Enhanced Visible-Light Photoelectrocatalytic Activity of p-n Junction BiOI/TiO_2 Nanotube Arrays, *J. Phys. Chem. C*, 2011, **115**, 7339–7346.

47 M. Law, L. E. Greene, J. C. Johnson, R. Saykally and P. Yang, Nanowire dye-sensitized solar cells, *Nat. Mater.*, 2005, **4**, 455–459.

48 C. Xu, P. Shin, L. Cao and D. Gao, Preferential Growth of Long ZnO Nanowire Array and Its Application in Dye-Sensitized Solar Cells, *J. Phys. Chem. C*, 2010, **114**, 125–129.

